Darbandi, Masood; Fatin, Ali; Bordbar, Hadi

Numerical study on NOx reduction in a large-scale heavy fuel oil-fired boiler using suitable burner adjustments

Published in:
Energy

DOI:
10.1016/j.energy.2020.117371

Published: 15/05/2020

Document Version
Peer-reviewed accepted author manuscript, also known as Final accepted manuscript or Post-print

Numerical study on NOx reduction in a large-scale heavy fuel oil-fired boiler using suitable burner adjustments*

Masoud Darbandi[a†], Ali Fatin[a], Hadi Bordbar[b]

[a] *Department of Aerospace Engineering, Sharif University of Technology, Tehran, Iran.*
[b] *Department of Civil Engineering, Aalto University, Finland.*

Abstract

A numerical framework was carefully developed to simulate the combustion of heavy-fuel-oil (HFO) in a large-scale boiler. The present numerical solutions were compared with the measured data of a laboratory benchmark test and on-site operational data of the chosen HFO-fired boiler. Next, the developed framework was used to perform the sensitivity analyses aiming to reduce the NO emission from the HFO-fired boiler without any adverse effect on its combustion performance. Practically, this study focused on re-adjustments of 24 working burners, which could control the combustion in the HFO-fired boiler. The early outcome showed that the boiler NO emission and its combustion performance could be controlled via the proper adjustments of air distributions within the three burners' stages and the swirl intensity. Although bigger mean droplet sizes and higher injection velocities reduced the NO emission considerably, it adversely led to much lower boiler's combustion efficiency. The present study eventually arrived at an optimal adjustment for the burners by reconsideration of the air distributions within the three burners' stages, the flame swirl intensity magnitude, and the fuel injection quality. The achieved

* Cite the article as: Masoud Darbandi, Ali Fatin, Hadi Bordbar, Numerical study on NOx reduction in a large-scale heavy fuel oil-fired boiler using suitable burner adjustments, Energy, Volume 199, 2020, 117371, https://doi.org/10.1016/j.energy.2020.117371.
†Corresponding author. Department of Aerospace Engineering, Sharif University of Technology, Tehran, P. O. Box 11365-11155, Postcode 14588-89694, Iran. Tel.: +98 21 6616-4644; Fax: +98 21 6602-2731. E-mail: darbandi@sharif.edu, URL: http://sharif.edu/~darbandi/

optimal adjustment reduced the amount of NO emission by 30%, while the combustion efficiency would remain unaffected.

Keywords: Combustion; heavy fuel oil; boiler; NO pollution; burner; simulation.

1. Introduction

Improving energy efficiency and reducing pollutant emission of combustion systems are among the most important issues to utilize world's limited energy resources in a sustainable way. The energy conversion performed through combustion in furnaces causes several pollutant emissions including carbon dioxide, carbon monoxide, and NO_x. Past investigations have already shown that the computational fluid dynamics (CFD) simulation is a powerful tool to analyze various physical phenomena occurring in laboratory and large-scale furnaces/boilers [1–8]. Literature shows that the simulation of combusting flow has been investigated in laboratory and large-scale furnaces/boilers from different aspects including the pollutants emission [5,9–15], the radiation heat transfer [1,2,16–21], and the turbulent combustion interaction [3,12,22,23]. Moreover, several recent researches have investigated the effect of particle fineness on the characteristics of gas-particle two-phase reactive flow in complex conditions of the industrial scale furnaces [8,13,24–29]. Essentially, the past researchers in reducing the pollution emission have focused on coal-based furnaces and boilers [4,5,8,13,23,30–33].

The heavy fuel oil (HFO)-fired boilers are considered one of the most pollutant boiler types in terms of NO_x and soot emissions. In some countries, the solution of demolishing these units is not likely or possible, so the alternative is the imposition of the necessary amendments to enhance their environmental-friendly performance. Recent researches have shown that the air swirl intensity [2,15], recycling of flue gas into the combustion air [34], and fuel injection quality [27,28] could affect the temperature field and NO_x emission within a large-scale furnace. There

are several techniques to control the NO_x emissions of the furnaces of which one basic approach is to adjust its burners properly. The furnaces of large-scale boilers are usually equipped with multiple burners suitably arranged inside the combustion zone. If these burners are not well adjusted, there will be flame-flame interference occurrence, which can dramatically elongate the overall length of flames inside the furnace and inevitably increase the chance of NO_x pollution in the stack [35]. To examine burner positioning effect on NO emission, Danon et al. [36] numerically studied different burner configurations in a multi-burner flameless combustion furnace. Their results showed that appropriate positioning of the burners led to higher temperature uniformities in the furnace, which resulted in lower thermal NO emission. Danon et al. [11] previously investigated in detail the effect of burner's adjustments on NO_x emission and efficiency in a natural gas-fired furnace.

A careful review of past related researches shows that there is limited information about the effect of burners' adjustments on the amount of NO_x emissions and overall combustion performance in large-scale HFO-fired furnaces. In present research, a numerical approach is used to reduce the NO_x emissions from an HFO-fired boiler by proper adjustments of its 24 burners. As known, NO_X is a generic term for the nitrogen oxides, namely nitric oxide (NO), nitrous oxide (N_2O) and nitrogen dioxide (NO_2). The past published researches in pollutant formation in full scale utility combustion systems have shown that N_2O and NO_2 have less contribution to pollutions compared with NO [37,38]. Hence, only the nitric oxide (NO) concentration is studied in the present study and NO_2 and N_2O are confidently neglected. Furthermore, three mechanisms of NO formation, including thermal, fuel, and prompt mechanisms are considered to predict NO concentration. To provide full sensitivity analyses on the effect of burners' adjustments on NO emission, this study carefully investigates the effects of swirl intensity, the

distribution of air among the three stages of burners, the droplet's sizes, and the injection velocity and monitors the amount of NO release from the large-scale boiler. Eventually, an optimal adjustment is suggested to minimize the NO pollution while the combustion efficiency would remain unaffected.

2. The Governing Equations and Numerical Models

2.1. The fluid flow governing equations

The governing equations for turbulent reacting flow with spray consist of the conservations of mass, momentums, energy, turbulence quantities, moments of mixture fraction, and droplet dispersion. The Favre averaged conservation equations for steady turbulent non-premixed flame are given by [39]

$$\frac{\partial}{\partial x_i}(\bar{\rho}\tilde{u}_i) = \bar{S}_m \tag{1}$$

$$\frac{\partial}{\partial x_i}\left(\bar{\rho}\tilde{u}_i\tilde{u}_j\right) + \frac{\partial \bar{p}}{\partial x_i} = \frac{\partial}{\partial x_i}\left(\bar{\tau}_{ij} - \bar{\rho}\widetilde{u_i^{"}u_j^{"}}\right) + \bar{S}_{u,i} \tag{2}$$

$$\frac{\partial}{\partial x_i}\left(\bar{\rho}\tilde{u}_i\tilde{Z}\right) = \frac{\partial}{\partial x_i}\left(\overline{\rho \mathrm{D}\frac{\partial Z}{\partial x_\iota}} - \bar{\rho}\widetilde{u_\iota^{"}Z^{"}}\right) + \bar{S}_{vapor} \tag{3}$$

$$\frac{\partial}{\partial x_i}\left(\bar{\rho}\tilde{u}_i\widetilde{Y_k}\right) = \frac{\partial}{\partial x_i}\left(\overline{\rho \mathrm{D}_k\frac{\partial Y_k}{\partial x_\iota}} - \bar{\rho}\widetilde{u_\iota^{"}Y_k^{"}}\right) + \bar{\dot{\omega}}_{reac} \qquad for \;\; k = 1, N \tag{4}$$

In these equations, the variable $\tilde{u}_i$ (i=1-3) denotes the velocity component in the x_i-direction, $\bar{\tau}_{ij}$ the viscous stress tensor, $\bar{\rho}$ the density, and $\bar{p}$ the hydrostatic pressure. The mixture fraction is defined as $\tilde{Z} = (sY_F - Y_{O_2} + Y_{O_2}^0)/(sY_F^0 + Y_{O_2}^0)$, where the parameters Y_F and Y_{O_2} respectively denote the fuel and oxygen mass fractions, Y_F^0 is the fuel mass fraction in fuel stream, and $Y_{O_2}^0$ is the oxygen mass fraction in oxidizer stream. The parameter s is stoichiometric mass ratio and is

defined as $\left[(\nu_{O_2}M_{O_2})/(\nu_F M_F)\right]$, where $\nu_{O_2}$and ν_F are the stoichiometric coefficient and M_{O_2} and M_F the molecular weights of oxygen and fuel, respectively. The molecular diffusion follows the Fick's law and the molecular diffusivities $\mathcal{D}_k$ are equal for all species ($\mathcal{D}_k = \mathcal{D}$). The source terms of above equations are given by the source term vector of ($\bar{S}_m, \bar{S}_{u,i}, \bar{S}_{vapor}, \bar{\dot{\omega}}_{reac}$). The turbulent Reynolds stresses $\widetilde{\bar{\rho}u_i''u_j''}$ are generally described using the turbulence viscosity assumption proposed by Boussinesq. It is written as

$$\widetilde{\bar{\rho}u_i''u_j''} = -\mu_t\left(\frac{\partial\tilde{u}_i}{\partial x_j}+\frac{\partial\tilde{u}_j}{\partial x_i}-\frac{2}{3}\delta_{ij}\frac{\partial\tilde{u}_k}{\partial x_k}\right)+\frac{2}{3}\bar{\rho}k \tag{5}$$

where μ_t denotes the turbulent dynamic viscosity, k the turbulent kinetic energy, and δ_{ij} the Kronecker delta.

2.2. Turbulence model

In present study, two-equation realizable k-ε model is used to closure the turbulent viscosity μ_t [40]. This model has been proved to be reliable enough in numerical modeling of turbulent flow fields in large-scale industrial applications [2,15,27]. Two transport equations are solved for the turbulent kinetic energy (k) and turbulent dissipation rate (ε). The standard values for the model constants are $C_{1\varepsilon} = 1.44$, $C_2 = 1.9$, $\sigma_k = 1.0$, and $\sigma_\varepsilon = 1.2$. To resolve the viscous effects in near wall zone, the standard wall functions are used here [41].

2.3. Disperse phase description

The Lagrangian approach is used to solve droplets motion in the continuous phase. Evaluating the ratio of droplet relaxation time (τ_p) to the period between two consequent collisions (τ_C), it provides an estimate how much the spray is dilute/dense. The flow can be considered dilute if $\tau_p/\tau_C < 1$. The droplet relaxation time is evaluated from $\tau_p = \rho_p d_p^2/18\mu$

[42], where μ is the dynamic viscosity coefficient of the carrier phase, ρ_p its droplet density, and d_p its droplet diameter. The Abrahamson's suggestion [43] is used for the droplet collision frequency calculation. In this study, we arrive at $\tau_p/\tau_C \approx 0.1$ considering a spray volume fraction about 10^{-5} and a droplet mean diameter less than $150\,\mu m$ in the boiler. Hence, the spray is dilute and the droplet's motion is controlled by the fluid forces (aerodynamic forces) rather than collisions. Considering only drag force and gravity effects, we solve the following equation to predict the droplets' trajectories:

$$\frac{d\vec{u}_p}{dt} = \frac{18\mu}{\rho_p d_p^2}\frac{C_d Re_p}{24}\left(\vec{u} - \vec{u}_p\right) + \frac{\vec{g}(\rho_p - \rho)}{\rho_p} \tag{6}$$

where $\vec{u}_p$ denotes the droplet's velocity vector, $\vec{g}$ the gravitation, and C_d the drag coefficient. The relative droplet Reynolds number is calculated from $Re_p = \rho d_p|\vec{u} - \vec{u}_p|/\mu$. To determine the drag coefficient of droplets (C_d), we use a dynamic drag model that accounts for the distortion effect of droplet [44]. Therefore, the drag coefficient is calculated from $C_d = C_{d,sphere}(1 + 2.635y)$, where y represents the droplet distortion. This equation states that the drag coefficient varies linearly between that of a sphere and a value of 1.52, which corresponds to the disk drag coefficient [44]. Here, a one-way coupling is considered to predict the interaction between the droplets and turbulent flow. The stochastic tracking approach is used to predict the effect of turbulent fluctuations on droplets' trajectory. Hence, the trajectory of droplets is predicted using the instantaneous value of the fluctuating gas velocity ($u = \bar{u} + u'$). The integral time for predicting droplets path is the minimum of the eddy lifetime and the droplet eddy crossing time [45]. Assuming the conditions of the current boiler, the Weber and Ohnesorge numbers become about 30 and 0.2, respectively. Therefore, the TAB breakup model, proposed by O'Rourke and

Amsden [46], would provide satisfactorily good prediction for breakup of droplets. The values $C_k = 8$, $C_b = 0.5$, and $C_d = 10$ are used as the coefficients of the TAB model [47].

The heat balance equation for droplets, i.e., the effects of mass transfer and the convective and radiative heat transfers, is given by

$$m_p c_p \frac{dT_p}{dt} = hA_p\left(T_\infty - T_p\right) + \frac{dm_p}{dt} h_{fg} + \varepsilon_p A_p \sigma(\theta_R^4 - T_P^4) \tag{7}$$

where variable m_p represents the droplet's mass, c_p its heat capacity, T_p its temperature, ε_p its emissivity factor, and A_p its surface area. Furthermore, θ_R denotes the radiation temperature, h the convective heat transfer coefficient, h_{fg} the specific latent heat, and σ the Stefan-Boltzmann constant. It is assumed that the thermal resistivity of droplets is negligible and each droplet has a uniform temperature. Hence, the convective heat transfer coefficient (h) is calculated using the modified Nusselt number as follows [48]:

$$Nu = hd_p/K_\infty = (\ln(1 + B_T)/B_T)(2.0 + 0.6Re_p^{\frac{1}{2}} Pr^{\frac{1}{3}}) \tag{8}$$

where, Nu is the Nusselt number, K_∞ the thermal conductivity of the carrier phase, B_T the Spalding heat transfer number, and Pr the Prandtl number. In the second term on the right-hand-side of Eq. (7), the vaporization rate (dm_p/dt) is calculated using $dm_p/dt = K_c A_p \rho_\infty \ln(1 + B_m)$, where the mass transfer coefficient (K_c) is obtained from the Sherwood number correlation as follows [49]:

$$Sh_{AB} = K_c d_p / D_{i,m} = 2.0 + 0.6Re_p^{\frac{1}{2}} Sc^{\frac{1}{3}} \tag{9}$$

where $D_{i,m}$ denotes the bulk diffusion coefficient with a value of 3.79×10^{-6} m^2/s [50], and Sc the Schmidt number.

The third term on the right-hand-side of Eq. (7) represents the radiative source term of the droplet. The radiation temperature is obtained from $\theta_R = (G/4\sigma)^{1/4}$, where G represents the incident radiation. When the droplet reaches the boiling temperature, the droplet temperature becomes constant. Therefore, the left-hand-side of Eq. (7) vanishes and the mass transfer rate during boiling is calculated from

$$-\frac{\mathrm{d}m_p}{\mathrm{d}t}h_{fg} = hA_p\left(T_\infty - T_p\right) + \varepsilon_p A_p \sigma(\theta_R^4 - T_P^4) \tag{10}$$

The evaporated liquid is considered as a source term in the gas phase species equations. The source terms $\bar{S}_m$, $\bar{S}_{u,i}$, and $\bar{S}_{vapor}$ (see Eqs. (1-3)) specify the interaction of mass and momentum between the droplets and the carrier flow [51,52].

2.4. Combustion model

Assuming infinitely fast chemistry with a unit Lewis number, the non-premixed turbulent flame is modeled based on the mixture fraction and the prescribed probability density function (pdf) method. In fact, for infinitely fast chemistry, the instantaneous mass fractions (Y_k) and temperature (T) are directly linked to the mixture fraction (Z). The pdf shape of the mixture fraction is supposed to be the β function, i.e. a clipped Gaussian. The chemical composition of current HFO fuel is $C_{12.13}H_{20.94}N_{0.004}S_{0.0262}$, which is obtained from the elemental composition of consumed HFO. The chemistry calculations and the pdf integrations are performed assuming the chemical equilibrium between 20 different species including C, H, S, N, and O as the HFO constituents, N_2 and O_2 as the air, CO_2, H_2O, CO, and H_2 as the product species, and CH_2, CH_4,

C_2H_2, C_2H_4, C_4H, C_4H_2, C_6H_6, OH, and HCN as the intermediate species. Table 1 presents the global reaction mechanism based on Park et al [53].

Table 1. Reaction mechanism rate constants in form of $k_f = AT^{\beta}\exp\left(-\frac{E_A}{R_u T}\right)$, the units are moles, cubic centimeters, seconds, Kelvins, and calories/mole.

Category	Reaction mechanism		A	β	E_A
Fuel pyrolysis	$C_{12.13}H_{20.94}N_{0.004}S_{0.0262} \rightarrow equilibrium\ mixture$		4.38×10^{12}	0.00	4.13×10^{4}
Nitric oxide	-Thermal NO [54]:				
	$O + N_2 \leftrightarrow N + NO$	*f **r	1.8×10^{8} 3.8×10^{7}	0.00 0.00	3.18×10^{5} 3.53×10^{3}
	$N + O_2 \leftrightarrow O + NO$	f r	1.8×10^{4} 3.81×10^{3}	1.00 1.00	3.89×10^{4} 1.73×10^{5}
	$N + OH \leftrightarrow H + NO$	f r	7.1×10^{7} 1.7×10^{8}	0.00 0.00	3.74×10^{3} 2.03×10^{5}
	- Fuel and prompt NO [55]:				
	$HCN + O \leftrightarrow NCO + H$	f	1.38×10^{4}	2.64	4.98×10^{3}
	$NCO + H \leftrightarrow CO + NH$	f	5.00×10^{13}	0.00	0.00
	$NH + H \leftrightarrow H_2 + N$	f	1.00×10^{14}	0.00	0.00
	$N + OH \leftrightarrow NO + H$	f	3.80×10^{13}	0.00	0.00
	$N + O_2 \leftrightarrow NO + O$	f	1.8×10^{4}	1.00	3.89×10^{4}
	$CH_3 + N \leftrightarrow H_2CN + H$	f	3.00×10^{13}	0.00	0.00
	$H_2CN + M \leftrightarrow HCN + H + M$	f	3.00×10^{14}	0.00	2.20×10^{4}
	$C + NO \leftrightarrow CN + O$	f	6.60×10^{13}	0.00	0.00
	$CN + H_2 \leftrightarrow HCN + H$	f	2.95×10^{5}	2.45	2.23×10^{3}
	$N + NO \leftrightarrow N_2 + O$	f	3.27×10^{12}	0.30	0.00
	$HCN + OH \leftrightarrow CN + H_2O$	f	1.45×10^{13}	0.00	1.09×10^{4}
Sulfur oxides	$H_2S + H \leftrightarrow SH + H_2$	f r	1.8197×10^{7} 9.3756×10^{6}	0.00 0.00	7.48×10^{3} 6.25×10^{4}
	$OH + H_2S \leftrightarrow H_2O + SH$	f r	1.3804×10^{2} 3.1045×10^{7}	0.00 0.00	3.74×10^{3} 1.22×10^{5}
	$SO + OH \leftrightarrow H + SO_2$	f r	1.6218×10^{8} 7.6913×10^{9}	0.00 0.00	2.56×10^{3} 1.18×10^{5}
	$SH + O \leftrightarrow SO + H$	f r	3.5481×10^{8} 2.9854×10^{9}	0.00 0.00	2.68×10^{3} 1.69×10^{5}
	$O + H_2S \leftrightarrow SH + OH$	f r	4.3651×10^{3} 9.8855×10^{8}	0.00 0.00	1.38×10^{4} 6.03×10^{4}
	$SO + O_2 \leftrightarrow SO_2 + O$	f r	4.4668×10^{5} 1.6634×10^{6}	0.00 0.00	2.70×10^{4} 7.61×10^{4}
	$SH + H + M \leftrightarrow H_2S + M$	f r	1.0964×10^{3} 8.6696×10^{14}	0.00 0.00	0.00 3.82×10^{5}
	$SO + O + M \leftrightarrow SO_2 + M$	f r	8.7096×10^{9} 1.9054×10^{14}	-1.80 0.00	0.00 2.20×10^{5}
	$SO_2 + O + M \leftrightarrow SO_3 + M$	f r	3.63×10^{2} 7.41×10^{14}	0.00 0.00	4.18×10^{3} 3.46×10^{5}

*f: forward reaction

**r: reverse reaction

2.5. NOx and SOx formation model

Table 1 provides the reaction mechanisms used in NOx and SOx calculations. To predict the formation rate of thermal NO, we use the extended Zeldovich mechanism [54] considering quasi steady-state assumption for the nitrogen atom concentration and the partial equilibrium assumption for the concentration of O atoms and OH radicals. The current M-380 HFO contains 0.19% (by weights) of nitrogen. HFO contains aromatic hydrocarbons [56] and nitrogen is bounded to alkyl benzenes and 2-ring, 3-ring aromatics. Hydrogen cyanide (HCN) appears to be the principle product under such circumstances [55]. Therefore, it is assumed that all the fuel nitrogen is released as HCN with the same evaporation rate as the liquid fuel and it takes part in the reaction mechanism of NO formation presented by Miller and Bowman [55]. Besides, the formation of prompt NO is caused by the HCN released from the reaction of hydrocarbon radicals (CHi) and molecular nitrogen (N_2). De Soete [57] describes the formation rate of HCN from this reaction in details. Similar to the fuel NO, the released HCN takes part in the Miller's reaction mechanism for NO formation.

Past experiments have shown that hydrogen sulfide (H_2S) is the dominant stable non-SO_2 product in combustion of fuels with fuel-bound sulfur [58]. So, it is assumed that all fuel-bound sulfur is released as H_2S. Table 1 also presents the details of reaction mechanism used for sulfur oxidation [58,59].

2.6. The soot formation model

A two equation semi-empirical soot formation model is implemented here. The transport equations for soot mass fraction and soot number density are solved in this model. They are given by

$$\vec{\nabla}.\left(\rho\vec{V}\dot{m}\right) = \vec{\nabla}.\left(\frac{\mu_e}{\sigma_{soot}}\vec{\nabla}\dot{m}\right) + S_{\dot{m}} \tag{11}$$

$$\vec{\nabla}.\left(\rho\vec{V}\dot{n}\right) = \vec{\nabla}.\left(\frac{\mu_e}{\sigma_{nuc}}\vec{\nabla}\dot{n}\right) + S_{\dot{n}} \tag{12}$$

The turbulent Schmidt numbers for the soot mass fraction (σ_{soot}) and the soot number density (σ_{nuc}) are taken 100. Considering the gas-phase nucleation and the free-molecular-regime coagulation for the soot particles, the source terms in Eqs. (11) and (12) are calculated from [60]

$$\begin{aligned} S_{\dot{m}} = {} & \underbrace{C_1\rho^2\left(\frac{Y_{C_2H_2}}{W_{C_2H_2}}\right)^2\frac{Y_{C_6H_3}}{W_{C_6H_3}}\frac{W_{H_2}}{Y_{H_2}}e^{-4378/T}}_{Nucleation} + \underbrace{C_2\rho^2\frac{Y_{C_2H_2}}{W_{C_2H_2}}\frac{Y_{C_6H_6}}{W_{C_6H_6}}\frac{Y_{C_6H_3}}{W_{C_6H_3}}\frac{W_{H_2}}{Y_{H_2}}e^{-6390/T}}_{Nucleation} \\ & + \underbrace{C_3\rho\frac{Y_{C_2H_2}}{W_{C_2H_2}}e^{-\frac{12100}{T}}(\pi\rho N_A\dot{n})^{1/3}\left(\frac{6\rho\dot{m}}{\rho_{soot}}\right)^{2/3}}_{Surface\ growth} - \underbrace{C_4\rho\frac{Y_{OH}}{W_{OH}}\sqrt{T}(\pi\rho N_A\dot{n})^{1/3}\left(\frac{6\rho\dot{m}}{\rho_{soot}}\right)^{2/3}}_{Oxidation} \end{aligned} \tag{13}$$

$$\begin{aligned} S_{\dot{n}} = {} & \underbrace{\frac{C_1}{M_p}\rho^2\left(\frac{Y_{C_2H_2}}{W_{C_2H_2}}\right)^2\frac{Y_{C_6H_3}}{W_{C_6H_3}}\frac{W_{H_2}}{Y_{H_2}}e^{-4378/T}}_{Nucleation} + \underbrace{\frac{C_2}{M_p}\rho^2\frac{Y_{C_2H_2}}{W_{C_2H_2}}\frac{Y_{C_6H_6}}{W_{C_6H_6}}\frac{Y_{C_6H_3}}{W_{C_6H_3}}\frac{W_{H_2}}{Y_{H_2}}e^{-6390/T}}_{Nucleation} \\ & - \underbrace{\frac{1}{N_A}\sqrt{\frac{24RT}{\rho_{soot}N_A}}(\rho N_A\dot{n})^{11/6}\left(\frac{6\rho\dot{m}}{\pi\rho_{soot}}\right)^{1/6}}_{Coagulation} \end{aligned} \tag{14}$$

The constants of Eqs. (13-14) are taken as $C_1 = 1016 \times 10^{8.88}\ s^{-1}$, $C_2 = 1424 \times 10^{9.50}\ s^{-1}$, $C_3 = 11700\ kg\ m\ kmol^{-1}s^{-1}$, $C_4 = 4.2325\ kg\ m\ kmol^{-1}K^{-1/2}s^{-1}$ and $\rho_{soot} = 2000\ kg/m^3$, $M_p = 144\ kg/kmol$, and $N_A = 6.022045 \times 10^{26} kmol^{-1}$.

2.7. Radiative heat transfer model

Considering the brilliant flame condition for HFO and high level of temperature in the furnace, the effect of thermal radiation must be included in the temperature field calculations. The finite-volume scheme is used to solve the radiative heat transfer equation [61,62]. Solid angle discretization is defined as Θ×φ, where Θ and φ, i.e. the number of divisions in the polar and azimuthal angles of one octant of 4π steradian, equal two, which causes 32 independent directions. The SLW model coupled with a modified reference approach [63] is used to obtain the gas radiation properties. This method combines the SLW model with a modified reference approach to remedy the high sensitivity of classical SLW method to the reference temperature magnitude in non-isothermal combustion fields. The effect of soot on thermal radiation is included by defining the total absorption coefficient as the sum of the absorption coefficients of gas (k_g) and soot (k_s). The absorption coefficient of soot is calculated from $k_s = 3.8322 C_0 \nu_s T / C_2$, where C_0 and C_2 are the model constants [64].

3. Boiler Description and Operating Conditions

Figure 1(a) shows a schematic of the current studied boiler. There are four Rankine cycle units in 1300 MW Shazand thermal power plant, which is located in Arak, Iran. Each unit has one subcritical natural circulation dual-fuel boiler, whose 24 burners are located on its opposite walls. The boiler is 30 m in height, 13.4 m in width, and 10.8 m in depth. The inlet of flue gas recirculation system has dimensions of 13.4 × 1.2 m and is located at the bottom of boiler. The percentages of recirculated flue gas can be determined according to the unit's load. Table 2 presents details of operating condition at the maximum continuous rating load condition (MCR). The fuel and air are evenly distributed between 24 burners. Figure 1(b) shows a schematic of dual-fuel swirl burners. Each burner has three stages of air supply and equipped with air swirlers. The air stages are introduced as primary, secondary, and tertiary air ducts in Fig. 1(b). The

primary air swirler is stationary, but the secondary and tertiary air swirlers can move in axial direction to adjust the intensity of swirled air. Burner's operating condition at the MCR is presented in Table 2. The HFO gun is located at the centerline of burner equipped with an adopted steam atomizing nozzle to improve the spray atomization of HFO. Figure 1(c) shows the layout of the burners and their swirling directions. The layout of swirl directions is symmetrical relative to the width and depth of boiler. The symmetrical layout helps to greatly simplify the computational domain.

Table 2. Operating condition at the MCR.

Furnace		**Burners**	
Power product (MW)	325	Primary air flow (t/h)	1.31
Main steam flow (t/h)	1040	Primary air swirl ratio*	1
Drum pressure (MPa)	18.6	Secondary air flow (t/h)	11.14
Excess air (%)	15	Secondary air swirl ratio	0.85
Air temperature (˚C)	287	Tertiary air flow (t/h)	0.65
Fuel consumption (t/h)	73.8	Tertiary air swirl ratio	1.65
Fuel temperature (˚C)	118	Atomizing steam pressure (MPa)	1.07
Flue gas (% of exhaust)	30.8		
Flue gas temperature (˚C)	347		

*Swirl ratio: the ratio of tangential velocity to the axial velocity

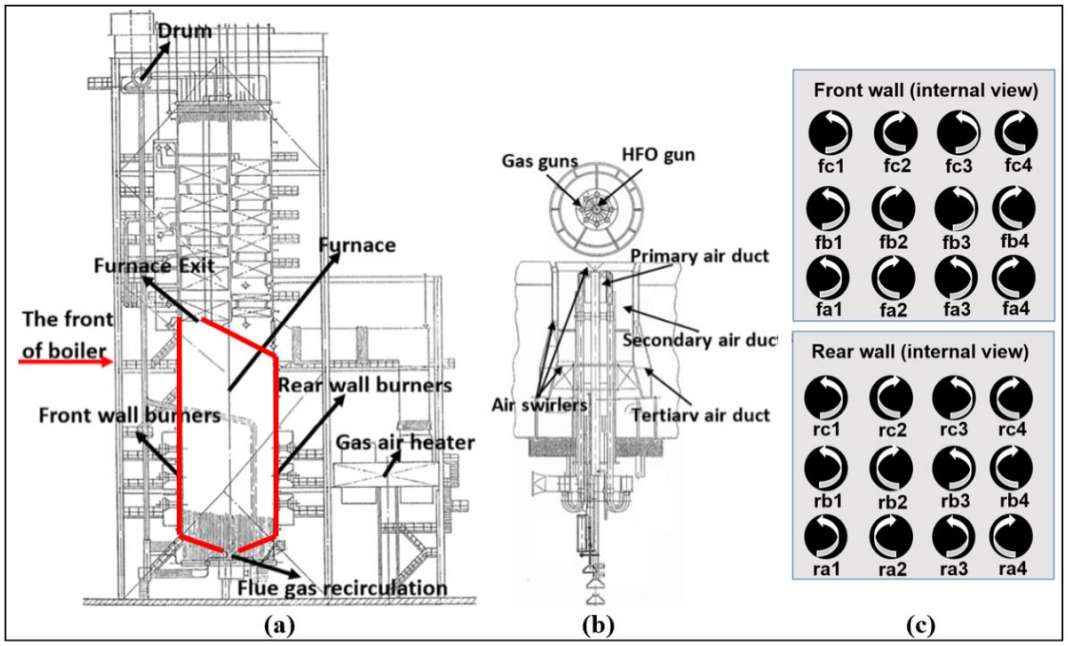

Fig. 1. The HFO-fired boiler configuration: a) schematic of the boiler, b) schematic of the swirling burners, and c) the layout of burners and their swirl directions.

According to the data collected in Shazand thermal power plant, the fuel consumed in boiler is M-380 HFO. Table 3 presents the analysis of this fuel.

Table 3. M-380 HFO composition and analysis.

Ultimate analysis (wt. %)					
C	H	S	O	N	ash
85.42	9.88	2.81	1.7	0.19	0.15
Proximate analysis (wt. %)					
Ash	Moisture	Fixed carbon	Volatile	Lower heating value (MJ/Kg)	Higher heating value (MJ/Kg)
0.15	-	1.6	98.25	38.84	40.53
Physical properties					
Density (Kg/m^3)		Kinematic viscosity (m^2/s)		Flash point (°C)	
997		7.2×10^{-5}		110	

4. Computational Method

The current research group has already developed various cell-face schemes, finite-volume (FV) methods, and CFD algorithms and that they have implemented them in a general computational framework to solve various flow problems including various reacting flow cases. Darbandi and Schneider [65] used the finite-volume-based finite-element (FVE) method and extended an analogy to solve compressible flows using pure pressure-based incompressible algorithms. This method was basically a dual-purpose algorithm. This hybrid FVE method was later extended to solve laminar flames [66], turbulent flames [67], and coupled turbulent flow and aerosol-combustion dynamics [68]. Ebrahimi-Kebria et al. [69] extended this pressure-based algorithm to simulate low Mach laminar mixing and reacting flow problems. The basic FVE method was further extended to account for combined convection-radiation heat transfer in participating media [62]. There were also advancements to calculate the thermal radiation transfer in combustion fields using advanced non-gray radiation models [21,29,70–73]. A detailed chemistry model was also implemented to improve the accuracy of turbulent reacting flow predictions [70]. This computational frame was further extended to take into account for the predictions of soot and other air pollutants in special applications such as furnaces and heavy duty steam generators [74], and jet propulsion-fueled combustors [75]. The current research benefits from these past experiences and develops a computational framework to solve the reacting flow field in a large scale HFO-fired boiler.

4.1. The numerical approach

Assuming a newtonian fluid, Eqs. (1-4) can be compacted into

$$\frac{\partial \boldsymbol{F}(\boldsymbol{q})}{\partial x}+\frac{\partial \boldsymbol{G}(\boldsymbol{q})}{\partial y}+\frac{\partial \boldsymbol{H}(\boldsymbol{q})}{\partial z}-\left(\frac{\partial \boldsymbol{F}'(\boldsymbol{q})}{\partial x}+\frac{\partial \boldsymbol{G}'(\boldsymbol{q})}{\partial y}+\frac{\partial \boldsymbol{H}'(\boldsymbol{q})}{\partial z}\right)=\boldsymbol{J} \tag{15}$$

where $\boldsymbol{q} = (\bar{p}, \tilde{u}_1, \tilde{u}_2, \tilde{u}_3, \tilde{Z}, \tilde{Y}_k)^T$ is the solution vector, $\boldsymbol{F}$, $\boldsymbol{G}$, and $\boldsymbol{H}$ are the convection flux vectors, $\boldsymbol{F}'$, $\boldsymbol{G}'$, and $\boldsymbol{H}'$ the diffusion flux vectors, and $\boldsymbol{J}$ the source term vector.

To follow the FVE discretization method, one needs to divide the computational domain into so many hexahedral elements. For the sake of simple description, the discretization is provided for a two-dimensional quadrilateral element in Fig. 2. There are four finite-elements in this figure. The unknown variables in the solution vector $\boldsymbol{q}$ are located at the element's nodes. The red lines are drawn by connecting the midpoints of each two opposite edges of an element to each other. The red lines divide each finite-element into four sub-rectangles. Each four sub-rectangles from four different adjacent finite-elements encompass one node. As seen in Fig. 2, these four sub-rectangles construct a control volume, which encompass this node. Each control-volume has eight control surfaces. These surfaces are the places, where the integrals of different convective and diffusive fluxes should be approximated. These integrals are approximated at the midpoint of each control surface. The midpoints of control surfaces are called integration points (ips).

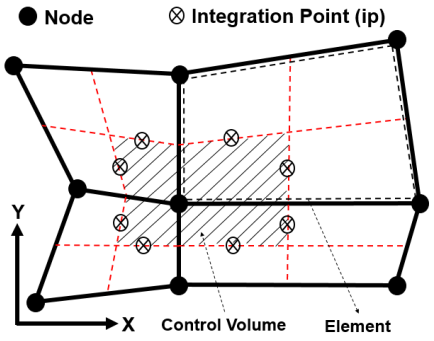

Fig. 2. Computational domain discretization strategy using finite-element grid.

Following Refs. [65–68,76], the FVE method is used to discretize the above governing equations. The finite-volume treatment of Eq. (15) yields

$$\sum_{j=1}^{8}\left[\boldsymbol{F}(\Delta S_x)+\boldsymbol{G}\left(\Delta S_y\right)+\boldsymbol{H}(\Delta S_z)\right]-\sum_{j=1}^{8}\left[\boldsymbol{F'}(\Delta S_x)+\boldsymbol{G'}\left(\Delta S_y\right)+\boldsymbol{H'}(\Delta S_z)\right]=\boldsymbol{J}(\Delta \boldsymbol{V_i}) \qquad (16)$$

where *i* indicates the finite-volume number, (ΔS) represents the areas of sub-surfaces around the chosen FV (the dashed lines), and (ΔV) is the volume (the shaded area) of FV. This discretization can be similarly applied to all other transport equations appeared in Sec. 2. For the governing equation terms with elliptic nature, i.e., $(\boldsymbol{F'},\boldsymbol{G'},\boldsymbol{H'})$, the finite-element shape functions are used to relate the ips to their corresponding nodal points located at the four vertices of the corresponding element. However, the treatment of convection terms, i.e., $(\boldsymbol{F},\boldsymbol{G},\boldsymbol{H})$, at the ips needs more sophisticated expressions which would be consistent with the fundamental convection-diffusion physics [65–67,76–78]. Here, the physical-influence upwind scheme PIS is utilized to establish the current FVE method [66–68]. Eventually, the source terms are completely approximated using the known values of the variables from the last iterative solution of the current nonlinear governing equations. This FVE discretization approach results in a 2nd-order accuracy for the diffusion terms and a 1st-2nd-order accuracy for the convection terms depending on the flow/grid Peclet number.

4.2. The boundary conditions

Considering the geometry of boiler and the swirl directions of the burners, see Fig. 1, one can apply the symmetry condition at the mid plane and simulate only one-half of the boiler. According to the operational conditions presented in Table 2, suitable boundary conditions can be applied at walls and burners. A zero mixture fraction is applied at oxidizer inlets, a specified exit pressure of 1 bar is specified at the outlet, and no-sleep velocity boundary condition is used at the furnace wall. It is assumed that the membrane walls are at the constant temperature of saturated water in the tubes. The saturated water is at drum pressure with a temperature of 360

°C. The emissivity factor is considered about 0.8 for the metal surface of the membrane walls. The droplet sizes were obtained by fitting the Rosin-Rammler exponential equation to droplet size distribution data. The 60 degrees solid cone fuel nozzle was tested in the quiescent atmosphere to provide the droplet size distribution data. The laser beam was placed at 11 radial positions 50 mm downstream of the atomizer tip and data sampling was collected for 30 seconds at each position. The range of diameters was between 1 to 180 μm. Fitting the data to above distribution, it leads to a mean diameter ($\bar{d}$) of about 53 μm and a spreading parameter (n) of about 1.56.

4.3. The computational mesh

As mentioned before, only one-half of the boiler is simulated here. Figure 3(a) partially shows the mesh distribution at the outer boundary of the 3D computational domain. For the grid dependency analysis, the temperature and velocity profiles were monitored along the white dashed-line shown in Fig. 3(a) using three different computational meshes with total numbers of 145,700, 572,355, and 1,019,900 non-uniform structured cells. The mesh was suitably refined in the flame zone adjacent to the front of burners. As shown in Figs. 3(b) and 3(c), the velocity and temperature distributions remain unchanged from the case with 572,355 cells to the one with 1,019,900 cells. Hence, the computational grid with 572,355 cells was chosen as the optimum computational mesh to carry out the current simulations.

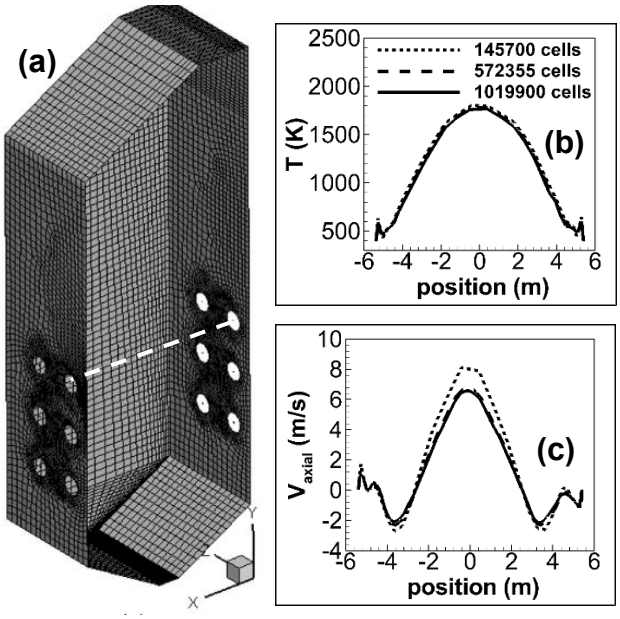

Fig. 3. Mesh refinement study in the boiler showing the temperature (b) and velocity (c) distributions along the white dashed-line shown in subplot (a) considering three mesh distributions.

5. Results and discussion

5.1. Validation of the extended numerical scheme

The experiment of Saario, et al. [79] is examined here to assess the capability of extended numerical scheme. This experiment investigated an HFO-fired swirl burner test in a down-fired cylindrical laboratory furnace. This test configuration was chosen because its basic flow features, i.e., highly swirling jets and combustion of fuel droplets, resemble those occurred inside a large-scale HFO-fired boiler. Figure 4(a) shows the two-dimensional axisymmetric swirl computational domain with 85000 non-uniform structured cells used to simulate the chosen experiment. The fuel and air flow conditions as well as the thermal conditions for walls are chosen similar to those practiced in the experiment [79]. The experimental data provide the distributions of volume fraction of various species at three axial locations of 20, 320, and 620

mm as shown in Fig. 4(a). Figure 4(b) shows the temperature contour in the domain for the swirl-stabilized spray flame. As seen, the maximum gas temperature reaches up to 2050 K in the furnace.

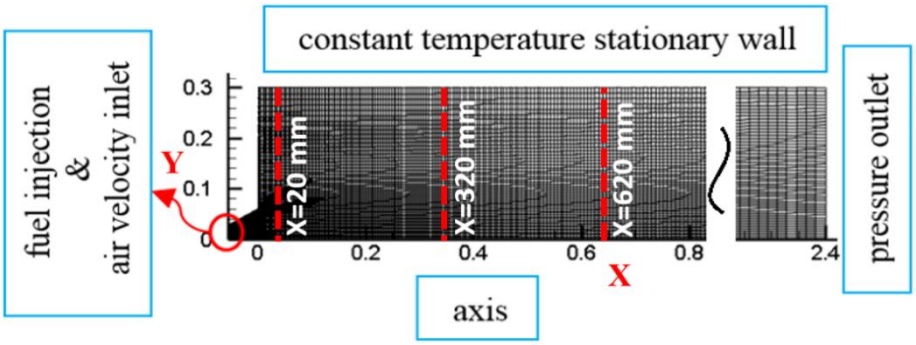

a) the computational domain sizes and the imposed boundary conditions

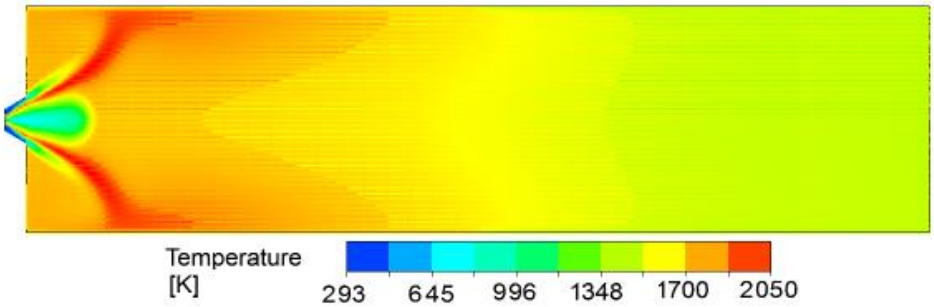

b) the contour plot of predicted temperature

Fig. 4. The computational domain geometry, imposed boundary conditions, and current simulation result.

Next, the present results are compared with the measured data for NO, O_2 and CO_2 volume fractions at different axial and radial locations inside the domain. Figure 5 shows the predicted profiles for the radial distributions of the volume fraction of NO at three axial downstream locations. As shown in this figure, although there are some discrepancies between the numerical predictions and the experimental data, especially at x=20 mm, there is generally satisfactory agreement between them. Moreover, Fig. 5 shows that the predicted NO volume fraction at x=620 mm is only 12% higher than the experimental data.

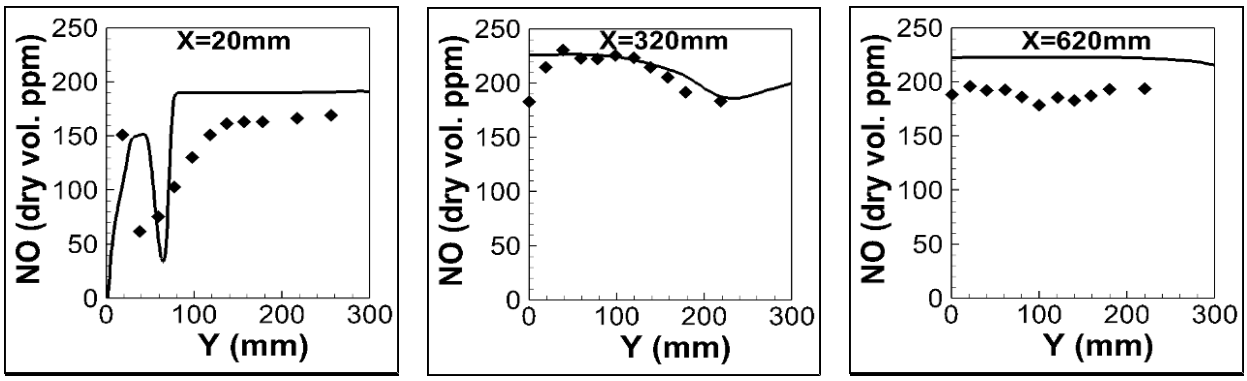

Fig. 5. The predicted radial profile of NO volume fraction at three axial distances of 20, 320, and 620 mm and comparison with the experiment of Saario, et al. [79].

Figures 6 and 7 show the predicted radial profile of volume fractions of O_2 and CO_2, respectively. As shown in these figures, the current simulation results provide satisfactory accuracy compared to the experimental data of Saario et al. [79]. However, it misses some of the trends observed in the experimental profiles, especially near the burner zone. It is because the chemistry would be controlled by the turbulence mixing if the fast kinetics assumption was applied here. Hence, the existing discrepancies can be attributed to deficiency of the turbulence modeling. It could be also attributed to non-precise definition of boundary conditions in numerical model, which was due to lack of information on experimental setup.

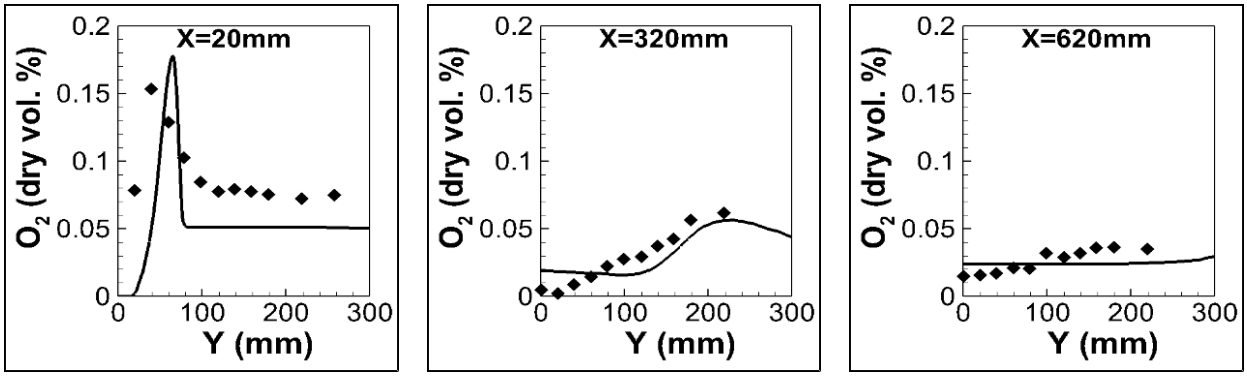

Fig. 6. The predicted radial profile of O_2 volume fraction at three axial distances of 20, 320, and 620 mm and comparison with the experimental data [79].

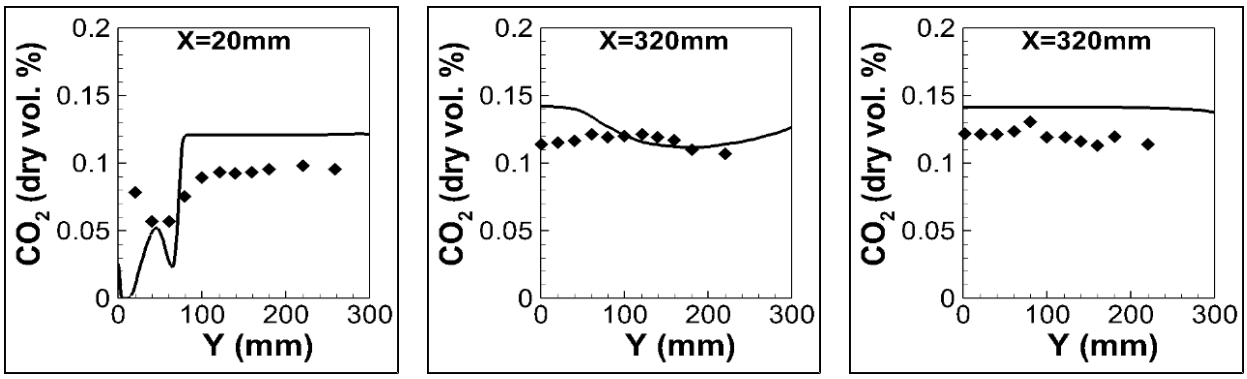

Fig. 7. The predicted radial profile of CO2 volume fraction at three axial distances of 20, 320, and 620 mm and comparison with the experimental data [79].

5.2. Comparison between numerical results and on-site measured data

The large HFO-fired boiler working in Shazand power plant is simulated at this stage using the computational framework presented in Secs. 2-4. Table 4 presents the simulation results and compares them with the on-site measured data. The available measured data were taken from this power plant at design working condition. The temperature and the species (CO_2, N_2, O_2 and NO) mole fractions were measured at the boiler exit imposing dry conditions at the furnace outlet. As seen in the last column of this table, the discrepancies between the measured data and the predicted results are less than 10% except for the NO concentration, which is about 11.8%. It is concluded that the current numerical framework can predict the combustion flow field in the current boiler with sufficient accuracy.

Table 4. Large-scale HFO-fired boiler simulation results (dry volume analyses) and comparison with the on-site measured data.

Parameter	Measured (%)	Simulation (%)	difference (%)
CO_2	12.7	11.76	7.4
N_2	82.9	83.73	1
O_2	4.4	4.28	2.7
NO (dry volume	398	445	11.8

ppm)			
Boiler exit temperature (˚C)	1241	1319	6.3

Figure 8 shows the temperature contours in two vertical and three horizontal cross sectional planes of the boiler. The maximum gas temperature in the boiler reaches up to 2100 K. The figure shows that the maximum gas temperature occurs in the upper regions of the boiler. Indeed, improper adjustment of burners has elongated the flame and resulted in flame interference at the higher elevations of boiler. Apparently, the proper adjustment of the burners can prevent such improper hot zones in higher levels of boiler and this can apparently result in lower thermal NO emissions. This will be examined and explained in more details in next section.

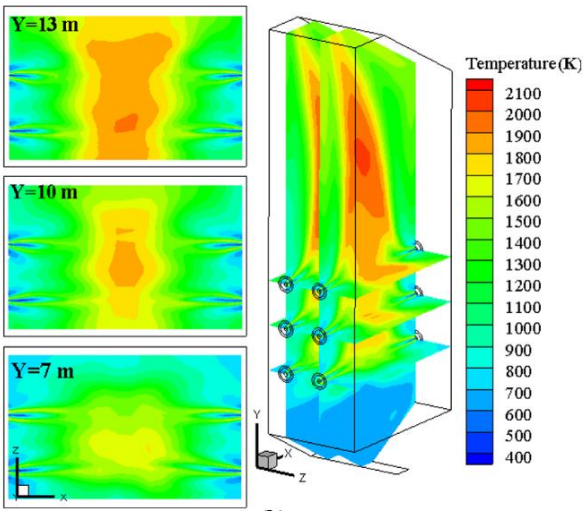

Fig. 8. The contour plots of predicted temperature field in two vertical and three horizontal planes across the burners installed at the side wall of boiler.

5.3. *The investigation to reduce the NO emission from the large-scale HFO-fired boiler*

Essentially, the flame configuration and temperature field inside the boiler, which in turn affect the amount of NO emission, depend on the adjustments of its burners. Table 5 introduces four important parameters, which can be used to adjust the burners' performance. The table also provides the range of variation for each parameter. To conduct a full sensitivity analysis on the

amount of NO emission from the 24 burners of boiler, the boiler is simulated for the entire range of each parameter.

Table 5. Burner's adjustable parameters.

Parameter	Ranges		
The secondary air swirl ratio	0.5-1.4		
Air distribution (primary, secondary, tertiary)%	(5-90-5)%	(10-85-5)%	(10-80-10)%
	(15-80-5)%	(15-75-10)%	(20-75-5)%
Spray's mean droplet size (μm)	25-150		
Fuel injection velocity (m/s)	20-120		

The combustion efficiency is defined as the ratio of predicted volume fraction of CO_2 to its maximum theoretical value at the furnace exit. The combustion efficiency of the boiler is affected by changing the burners' adjustments. Therefore, in addition to NO emission rate, it is important to take into account the combustion efficiency of boiler in our study. Figure 9 shows how the NO volume fraction and the combustion efficiency of boiler change with the changes in burners' adjustable parameters. Figure 9(a) shows the results for various air distributions among the three air's outlets of burners. The figure shows that the volume fraction of NO decreases by increasing the proportion of primary air from 5 to 20%. Nevertheless, by increasing the proportion of the tertiary air from 5 to 10%, the combustion efficiency dramatically decreases, which is a negative point. However, both NO volume fraction and combustion efficiency are in acceptable ranges for the case of (20-75-5)% air distributions. Figure 9(b) presents the effect of swirl ratio of secondary air on the NO volume fraction and the combustion efficiency of the boiler. As seen in this figure, the NO volume fraction is minimum at a swirl ratio of 1.2, while

the combustion efficiency has a moderate value of 80.5%. Alternatively, the minimum value of combustion efficiency would occur at a swirl ratio of about unity.

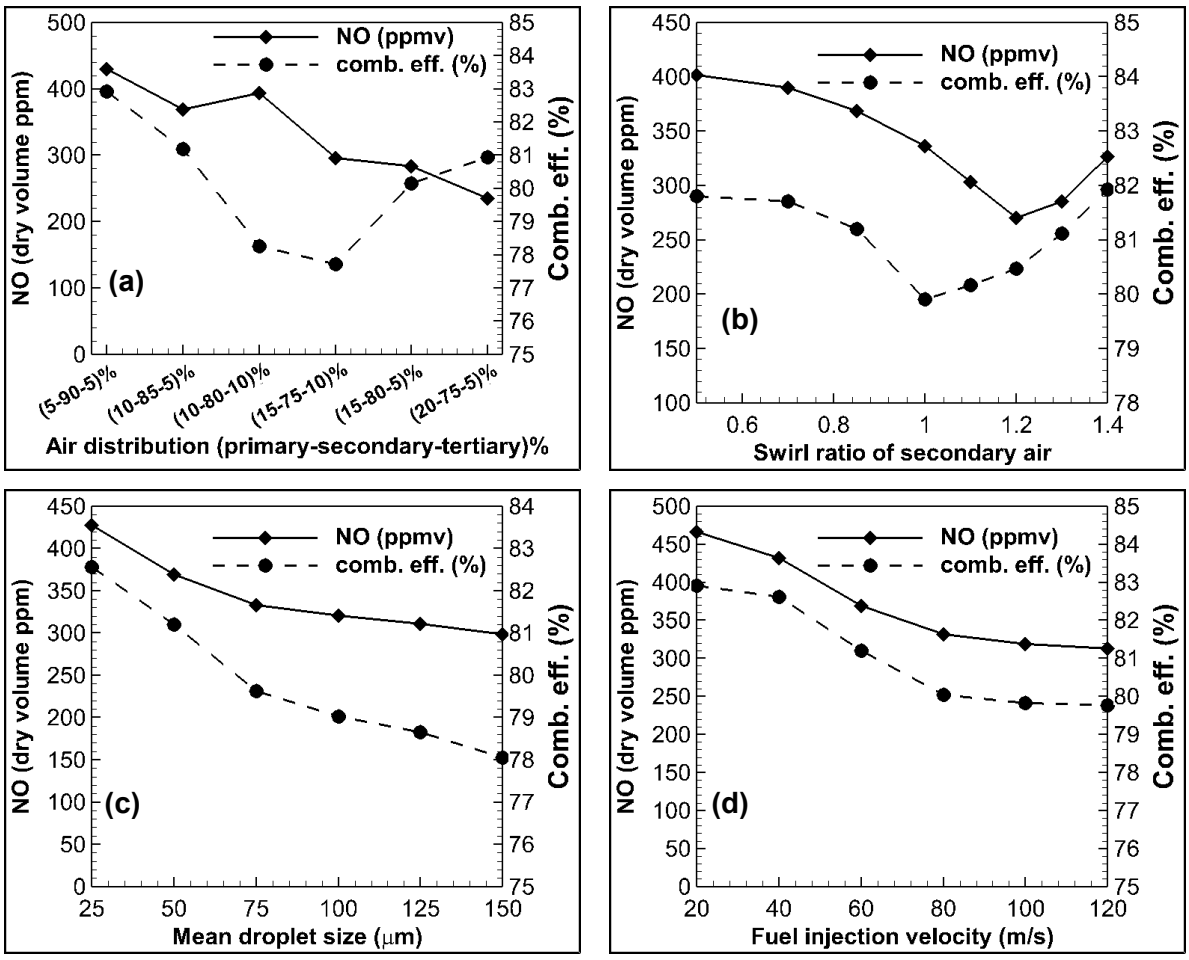

Fig. 9. Changes in NO volume fraction at the boiler exit and its combustion efficiency considering various a) air distributions between the three air stages of each burner, b) swirl ratios of the secondary air, c) mean droplet sizes, and d) fuel injection velocities.

Figure 9(c) shows the variations of NO volume fraction and combustion efficiency of the boiler with the changes in mean droplet size. According to this figure, the bigger mean droplet size choices lead to lower NO volume fraction and combustion efficiency of boiler. Similarly, Fig. 9(d) shows the effects of fuel injection velocity on NO volume fraction and combustion efficiency of the boiler. As seen, both the NO volume fraction and the combustion efficiency steadily decrease with the injection velocity augmentation.

Back to Fig. 9, Fig. 9(b) shows that there is an optimum, swirl ratio value between the lower and upper limits of the chosen swirl ratio range, which leads to a minimum NO emission. There might be a question why the optimum value is not achieved at the chosen lower or upper bounds. To answer this question, Figure 10 depicts the temperature contour at z=3.93 m plane considering several different swirl number values. The figure shows that the length of flame generally decreases as the swirl number increases, which is rational. This reduces the chance of strong interference between the flames of opposite burners. However, the figure also shows that the flames from the burners mounted on the opposite walls will combine and create either one large hot spot or two small hot spots depending on the swirl number value. The former and latter happen at lower and higher swirl number values, respectively. The figure indicates that the single hot zone grows as the swirl number increases; however, it breaks into two smaller zones with more increase in the swirl number. If the swirl number is increased further, the two separate hot zones also start growing. That is why the hot zone with a temperature higher than 1900 K is more limited for the case with swirl number of 1.2. In other words, the thermal NO emission would be minimal for the swirl number of 1.2.

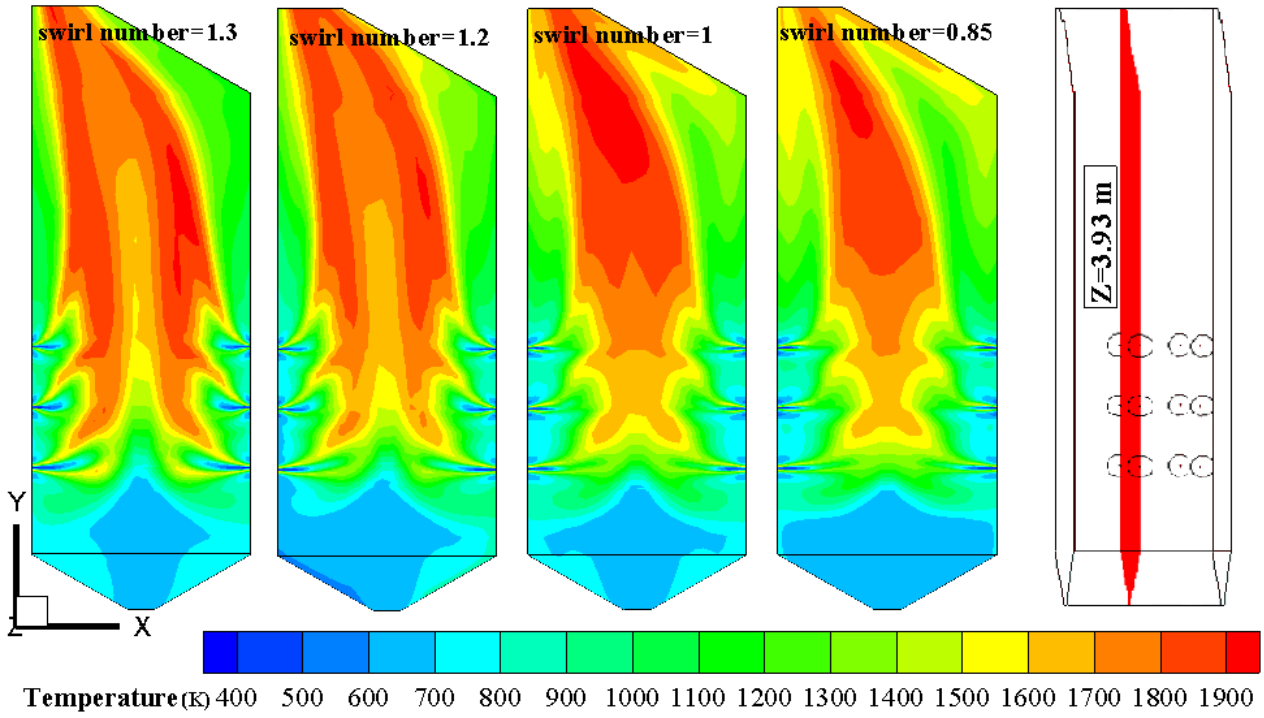

Fig. 10. Temperature contour at z=3.93 m plane considering various swirl number adjustments of 0.85, 1.0, 1.2, and 1.3.

Figure 11 shows the variation of mean gas temperature along the height of boiler considering various air distributions between the primary, secondary, and tertiary stages of burners. For the case of choosing (20-75-5)%, the gas temperature is relatively higher than the other cases at the elevations of 7, 10 and 13 m, where the burners are located. On the other hand, the gas temperature of this distribution gets close to those of other cases at elevations higher than 15 m. Indeed, increasing the primary air would provide better mixing and combustion at zones close to the burner, where the HFO diffusion flame is formed. This would avoid extensive hot zone at higher elevations and therefore would reduce the NO emission.

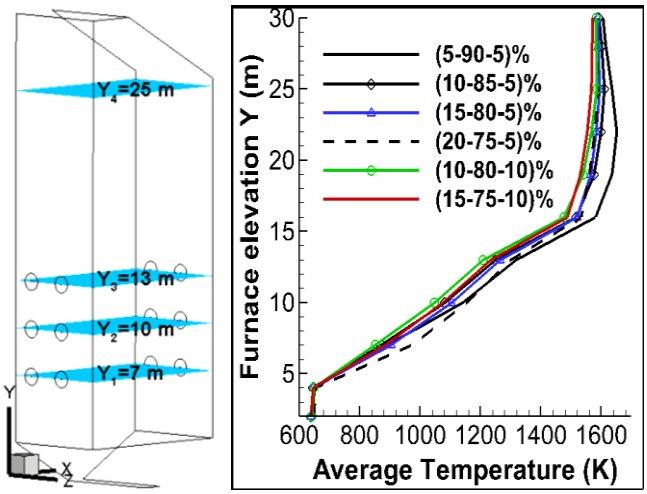

Fig. 11. Variation of mean gas temperature along the height of boiler considering various air distributions between the primary, secondary, and tertiary stages of burners.

Figures 9(c) and 9(d) showed that an increment in both the mean droplet size and injection velocity would decrease the NO volume fraction and the combustion efficiency of boiler, simultaneously. To explain this observation, Figures 12 and 13 demonstrate the fuel mean mixture fraction (f_{fuel}) contour plot considering various mean droplet sizes (25, 100, and 150 μm) and injection velocities (20, 60 and 120 m/s), respectively. Figure 12 presents the contour plots for an injection velocity of 60 m/s, which corresponds to the base condition. Also, Fig. 13 presents the contour plots considering a mean droplet size of 100 μm. These figures also demonstrate the flame fronts using the specific isoline value of the stoichiometric mixture fraction for heavy oil, i.e., f_{fuel}= 0.065. Figure 12 shows that the flame length for each burner increases by increasing the mean droplet size from 25 to 150 μm. It is because of achieving higher penetration length and evaporation time for the bigger droplets. Similarly, Fig. 13 shows that the higher the injection velocity is, the longer the flame of each burner will be. In the other words, a higher injection velocity increases the penetration length of droplets and consequently the flame length will be longer. Higher injection velocity values and larger droplet size magnitudes will cause the droplets to leave the mixing zone rapidly and this leads to fuel rich

region inside the boiler. Arriving at richer combustion conditions in the boiler, it will reduce the maximum flame temperature and will consequently prevent NO emission. However, it increases the unburned hydrocarbons and CO in the stack due to incomplete combustion occurrences. As a result, the combustion efficiency decreases by increasing the mean droplet size and injection velocity magnitudes, as predicted in Figs. 9(c) and 9(d) as well.

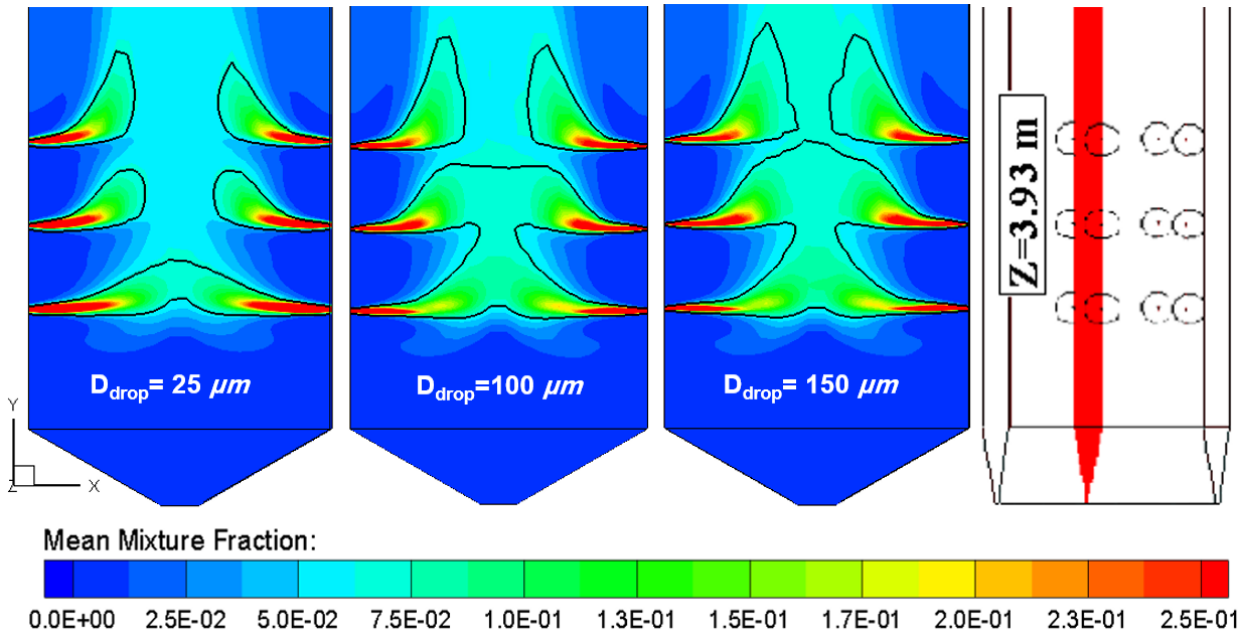

Fig. 12. The mixture fraction contour for heavy oil at z=3.93 m plane considering different mean droplet sizes of 25, 100, and 150 μm, the solid black lines demonstrate the isoline of the stoichiometric mixture fraction (f_{fuel}= 0.065).

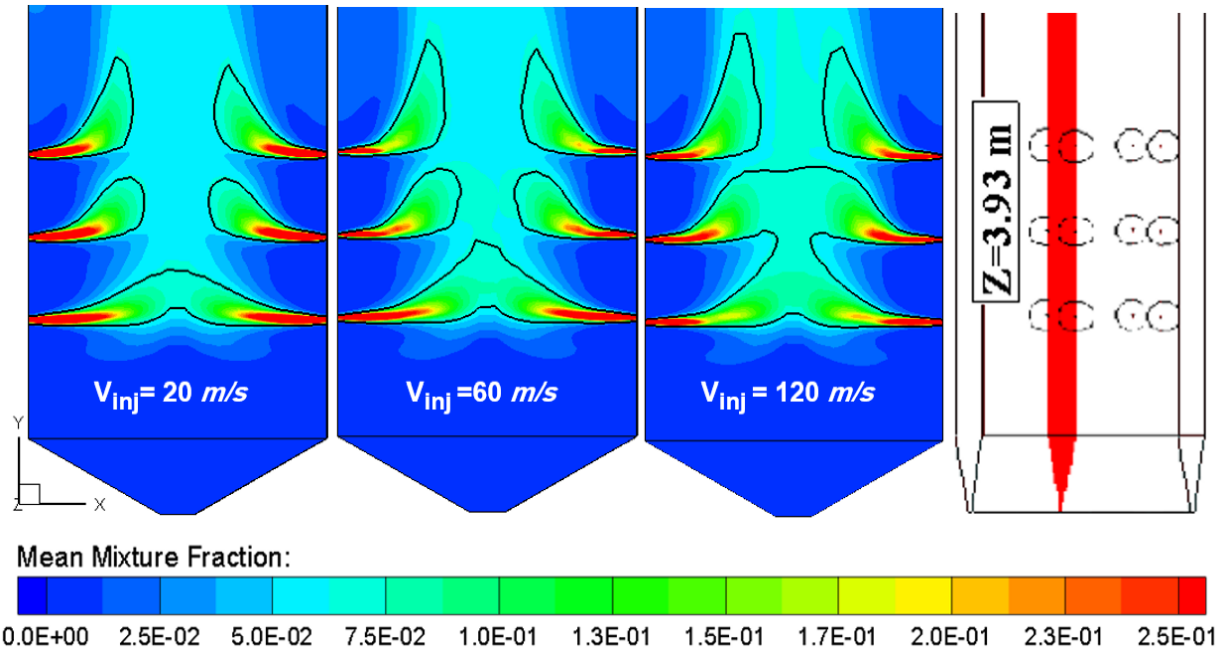

Fig. 13. The mixture fraction contour for heavy oil at z=3.93 m plane considering different injection velocities of 20, 60 and 120 m/s; the solid black lines demonstrate the isoline of the stoichiometric mixture fraction (f_{fuel}= 0.065).

Figure 14 shows the NO emission and combustion efficiency of the boiler for three selected burners' adjustments. These choices of adjustments are called current, setup 1, and setup 2. The "current" refers to the current burner adjustment in Shazand boiler and setups 1 and 2 refer to two new suggested adjustments for the burners, which apparently reduce the NO emission. The gradient method is used in setup 1 to determine the optimal conditions to minimize the NO emission. Accordingly, setup 1 considers a swirl number ratio of 1.18, the air distributions of (20-75-5)% for the (primary-secondary-tertiary) air stages, a mean droplet size of 77 μm, and an injection velocity of 88 m/s to possibly reduce the NO emission to a minimum value. Figure 14 shows that setup 1 provides suitable circumstances, in which the NO emission reduces to 188 ppmv. In other words, this setup results in more than 49% reductions in NO emission compared with the "current" adjustment. Despite a sound reduction in NO emission, the combustion efficiency drops to 74.5% and this would cause dramatic decrease in the power generation of the

corresponding thermal power plant cycle. Evidently, one major requirement in new burners' adjustments is to maintain the combustion efficiency of the furnace as before. Re-inspecting the various burners' working conditions and their adjustments in Fig. 9, one will eventually arrive at a combustion efficiency of 81% as a compromised value for the current simulated boiler. Considering this important point, one can conclude that the optimal burners' adjustments would be at a swirl ratio of 1.25, an air distribution of (20-75-5)%, a mean droplet size of 50 μm, and an injection velocity of 65 m/s. These new burners' adjustments are called setup 2. Figure 14 shows that the NO emission reduces to a minimum amount of 257 ppmv using setup 2. The good point is that this burner's adjustment does not deteriorate the combustion efficiency of HFO-fired boiler. Quantitatively, setup 2 results in 30% reductions in NO emission compared with the "current" situation; however, with the same combustion efficiency.

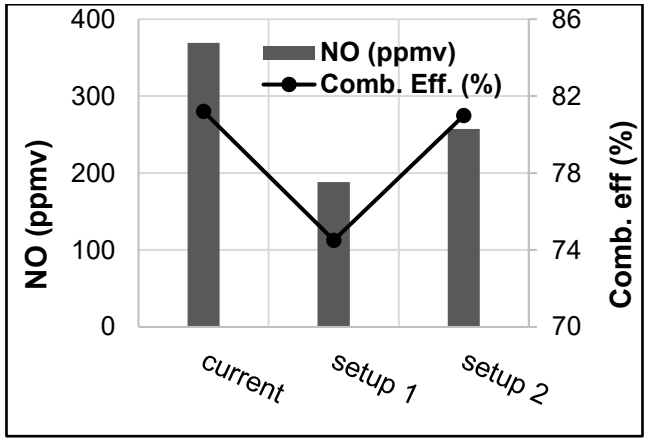

Fig. 14. The NO emission and combustion efficiency of the boiler for three selected burners' adjustments including current, setup 1, and setup 2.

6. Conclusions

A numerical framework was suitably extended to simulate the turbulent reactive flow in a large-scale heavy fuel oil (HFO)-fired boiler. The main objective of this work was to reduce the NO emission from an on-site boiler by prescribing new burners' adjustments while keeping its

combustion efficiency unaffected. Various adjustments of boiler's burners were investigated and their impacts on a number of significant parameters were studied. It was observed that the swirl ratio of the burner secondary air could have an optimum value to result in the minimum NO emission. Imposing very low and very high swirl number ratios, the flames would interfere by the opposite burners and the adjacent burners, respectively. Additionally, increasing the proportion of the primary air would decrease the NO emission, while increasing the proportion of the tertiary air would decrease the combustion efficiency. Furthermore, increasing the mean droplet size and/or injection velocity would decrease the NO volume fraction due to generating rich combustion conditions in the boiler furnace. Subsequently, it would results in more unburned hydrocarbons and CO species in the stack and consequently resulting in lower combustion efficiency. This research was eventually arrived at two new adjustments for the burners of this HFO-fired boiler based on the obtained results from the numerical analysis. They were called setups 1 and 2. Setup 1 reduced the NO volume fraction by 49% comparing with the original setup. However, it simultaneously caused a dramatic decrease in the combustion efficiency of boiler. In contrary, setup 2 provided better combustion efficiency; however, the NO emission for this setup was relatively higher than that of setup 1. Compared with the current adjustments of boiler's burners, setup 2 caused 30% reduction in NO emission, while the combustion efficiency remained almost unaffected. Therefore, setup 2 is suggested as the optimal burner adjustments for the chosen onsite boiler. This study can be equally followed up in other similar boilers to significantly reduce their NO emission without deteriorating their thermal efficiencies.

7. Acknowledgment

The authors would appreciate the support received from the Deputy of Research and Technology in Sharif University of Technology (SUT-RTD-96-073). The third author (H. B.) would like to acknowledge the support of Academy of Finland under Grant No 314487.

References

[1] Bordbar MH, Hyppänen T. Modeling of radiation heat transfer in a boiler furnace. Adv Stud Theor Phys 2007;1:571–84.

[2] Pourramezan M, Kahrom M, Passandideh-Fard M. Numerical investigation on the lifetime decline of burners in a wall-fired dual-fuel utility boiler. Appl Therm Eng 2015;82:141–51.

[3] Liu Y, Fan W, Li Y. Numerical investigation of air-staged combustion emphasizing char gasification and gas temperature deviation in a large-scale, tangentially fired pulverized-coal boiler. Appl Energy 2016;177:323–34.

[4] Adamczyk WP, Bialecki RA, Ditaranto M, Gladysz P, Haugen NEL, Katelbach-Wozniak A, et al. CFD modeling and thermodynamic analysis of a concept of a MILD-OXY combustion large scale pulverized coal boiler. Energy 2017;140:1305–15.

[5] Adamczyk WP, Isaac B, Parra-Alvarez J, Smith ST, Harris D, Thornock JN, et al. Application of LES-CFD for predicting pulverized-coal working conditions after installation of NOx control system. Energy 2018;160:693–709.

[6] Maakala V, Järvinen M, Vuorinen V. Optimizing the heat transfer performance of the recovery boiler superheaters using simulated annealing, surrogate modeling, and computational fluid dynamics. Energy 2018;160:361–77.

[7] Echi S, Bouabidi A, Driss Z, Abid MS. CFD simulation and optimization of industrial boiler. Energy 2019;169:105–14.

[8] Belošević S, Tomanović I, Crnomarković N, Milićević A. Full-scale CFD investigation of gas-particle flow, interactions and combustion in tangentially fired pulverized coal furnace. Energy 2019;179:1036–53.

[9] Fan JR, Liang XH, Chen LH, Cen KF. Modeling of NOx emissions from a W-shaped boiler furnace under different operating conditions. Energy 1998;23:1051–5.

[10] Xu M, Azevedo JLT, Carvalho MG. Modelling of the combustion process and NOx emission in a utility boiler. Fuel 2000;79:1611–9.

[11] Danon B, Swiderski A, De Jong W, Yang W, Roekaerts D. Emission and efficiency comparison of different firing modes in a furnace with four HiTAC burners. Combust Sci Technol 2011;183:686–703.

[12] Li Z, Liu G, Chen Z, Zeng L, Zhu Q. Effect of angle of arch-supplied overfire air on flow, combustion characteristics and NOx emissions of a down-fired utility boiler. Energy 2013;59:377–86.

[13] Kuang M, Li Z. Review of gas/particle flow, coal combustion, and NOx emission characteristics within down-fired boilers. Energy 2014;69:144–78.

[14] Gu M, Wang M, Chen X, Wang J, Lin Y, Chu H. Numerical study on the effect of separated over-fire air ratio on combustion characteristics and NOx emission in a 1000 MW supercritical CO2 boiler. Energy 2019;175:593–603.

[15] Zhou H, Meng S. Numerical prediction of swirl burner geometry effects on NOx emission and combustion instability in heavy oil-fired boiler. Appl Therm Eng 2019;159:113843.

[16] Bordbar MH, Hyppänen T. Multiscale numerical simulation of radiation heat transfer in participating media. Heat Transf Eng 2013;34:54–69.

[17] Bordbar MH, Myöhänen K, Hyppänen T. Coupling of a radiative heat transfer model and a three-dimensional combustion model for a circulating fluidized bed furnace. Appl Therm Eng 2015;76:344–56.

[18] Zhang X, Zhou J, Sun S, Sun R, Qin M. Numerical investigation of low NOx combustion strategies in tangentially-fired coal boilers. Fuel 2015;142:215–21.

[19] Bordbar MH, Hyppänen T. The correlation based zonal method and its application to the back pass channel of oxy/air-fired CFB boiler. Appl Therm Eng 2015;78:351–63.

[20] Zhang J, Ito T, Ito S, Riechelmann D, Fujimori T. Numerical investigation of oxy-coal combustion in a large-scale furnace: non-gray effect of gas and role of particle radiation. Fuel 2015;139:87–93.

[21] Bordbar H, Fraga GC, Hostikka S. An extended weighted-sum-of-gray-gases model to account for all CO2-H2O molar fraction ratios in thermal radiation. Int Commun Heat Mass Transf 2020;110:104400.

[22] Chen S, He B, He D, Cao Y, Ding G, Liu X, et al. Numerical investigations on different tangential arrangements of burners for a 600 MW utility boiler. Energy 2017;122:287–300.

[23] Gil A V, Zavorin AS, Starchenko A V. Numerical investigation of the combustion process for design and non-design coal in T-shaped boilers with swirl burners. Energy 2019;186:115844.

[24] Bordbar MH, Zamankhan P. Dynamical states of bubbling in vertically vibrated granular materials. Part I: Collective processes. Commun Nonlinear Sci Numer Simul 2007;12:254–72.

[25] Bordbar MH, Zamankhan P. Dynamical states of bubbling in vertical vibrated granular materials. Part II: Theoretical analysis and simulations. Commun Nonlinear Sci Numer Simul 2007;12:273–99.

[26] Bordbar MH, Hyppänen T. Simulation of bubble formation and heaping in a vibrating granular bed. Chem Eng Commun 2011;198:905–19.

[27] Bonefačić I, Wolf I, Blecich P. Improvement of fuel oil spray combustion inside a 7 MW industrial furnace: A numerical study. Appl Therm Eng 2017;110:795–804.

[28] Darbandi M, Fatin A, Schneider GE. Careful Parameter Study to Enhance the Effect of Injecting Heavy Fuel Oil Into a Crossflow Using Numerical Approaches. ASME 2018 5th Jt. US-European Fluids Eng. Div. Summer Meet., American Society of Mechanical Engineers; 2018, p. V002T09A016-V002T09A016.

[29] Isojärvi T, Bordbar H, Hostikka S. Spectrally resolved calculation of thermal radiation penetration into liquid n-heptane in pool fires. Int J Heat Mass Transf 2018;127:1101–9.

[30] Chen Z, Li Z, Zhu Q, Jing J. Gas/particle flow and combustion characteristics and NOx emissions of a new swirl coal burner. Energy 2011;36:709–23.

[31] Wang C, Liu Y, Zheng S, Jiang A. Optimizing combustion of coal fired boilers for reducing NOx emission using Gaussian Process. Energy 2018;153:149–58.

[32] Li Z, Miao Z. Primary air ratio affects coal utilization mode and NOx emission in lignite pulverized boiler. Energy 2019;187:116023.

[33] Tan P, He B, Zhang C, Rao D, Li S, Fang Q, et al. Dynamic modeling of NOX emission in a 660 MW coal-fired boiler with long short-term memory. Energy 2019;176:429–36.

[34] Zhu S, Venneker B, Roekaerts D, Pozarlik A, van der Meer T. Numerical investigation towards a HiTAC condition in a 9MW heavy fuel-oil boiler. 6th Eur. Combust. Meet., 2013.

[35] Baukal Jr CE. The john zink hamworthy combustion handbook: Volume 1-Fundamentals. CRC press; 2012.

[36] Danon B, Cho E-S, De Jong W, Roekaerts D. Numerical investigation of burner positioning effects in a multi-burner flameless combustion furnace. Appl Therm Eng 2011;31:3885–96.

[37] Muzio LJ, Montgomery TA, Samuelsen GS, Kramlich JC, Lyon RK, Kokkinos A. Formation and measurement of N2O in combustion systems. Symp. Combust., vol. 23, Elsevier; 1991, p. 245–50.

[38] Bowman CT. Kinetics of pollutant formation and destruction in combustion. Prog Energy Combust Sci 1975;1:33–45.

[39] Poinsot T, Veynante D. Theoretical and numerical combustion. RT Edwards, Inc.; 2005.

[40] Shih T-H, Liou WW, Shabbir A, Yang Z, Zhu J. A new k-ϵ eddy viscosity model for high reynolds number turbulent flows. Comput Fluids 1995;24:227–38.

[41] Launder BE, Spalding DB. The numerical computation of turbulent flows. Numer. Predict. flow, heat Transf. Turbul. Combust., Elsevier; 1983, p. 96–116.

[42] Schwarzkopf JD, Sommerfeld M, Crowe CT, Tsuji Y. Multiphase flows with droplets and particles. CRC press; 2011.

[43] Abrahamson J. Collision rates of small particles in a vigorously turbulent fluid. Chem Eng Sci 1975;30:1371–9.

[44] Liu AB, Mather D, Reitz RD. SAE Technical Paper 930072. SAE, Detroit 1993;1.

[45] Gosman AD, Loannides E. Aspects of computer simulation of liquid-fueled combustors. J Energy 1983;7:482–90.

[46] O'Rourke PJ, Amsden AA. The TAB method for numerical calculation of spray droplet breakup, SAE Technical Paper, 872089. Soc Automot Eng Warrendale, PA 1987.

[47] Marek M. The double-mass model of drop deformation and secondary breakup. Appl Math Model 2013;37:7919–39.

[48] Sazhin SS. Advanced models of fuel droplet heating and evaporation. Prog Energy Combust Sci 2006;32:162–214.

[49] Ranz WE, Marshall WR. Evaporation from drops. Chem Eng Prog 1952;48:141–6.

[50] Nieckele AO, Naccache MF, Gomes MSP. Combustion performance of an aluminum melting furnace operating with natural gas and liquid fuel. Appl Therm Eng 2011;31:841–51.

[51] Chrigui M, Sadiki A, Ahmadi G. Study of interaction in spray between evaporating droplets and turbulence using second order turbulence RANS modelling and a Lagrangian approach. Prog Comput Fluid Dyn an Int J 2004;4:162–74.

[52] Chrigui M, Gounder J, Sadiki A, Masri AR, Janicka J. Partially premixed reacting acetone spray using LES and FGM tabulated chemistry. Combust Flame 2012;159:2718–41.

[53] Park JK, Park S, Ryu C, Baek SH, Kim YJ, Park HY. CFD analysis on bioliquid co-firing with heavy fuel oil in a 400 MWe power plant with a wall-firing boiler. Appl Therm Eng 2017;124:1247–56.

[54] Hanson RK, Salimian S. Survey of Rate Constants in the N/H/O System, Combustion Chemistry, Gardiner, WC, Ed., Chapter 6 1984.

[55] Miller JA, Bowman CT. Mechanism and modeling of nitrogen chemistry in combustion. Prog Energy Combust Sci 1989;15:287–338.

[56] Speight JG. Production, properties and environmental impact of hydrocarbon fuel conversion. Adv. Clean Hydrocarb. Fuel Process., Elsevier; 2011, p. 54–82.

[57] De Soete GG. Overall reaction rates of NO and N2 formation from fuel nitrogen. Symp. Combust., vol. 15, Elsevier; 1975, p. 1093–102.

[58] Kramlich JC, Malte PC, Grosshandler WL. The reaction of fuel-sulfur in hydrocarbon combustion. Symp. Combust., vol. 18, Elsevier; 1981, p. 151–61.

[59] Hunter SC. Formation of SO3 in gas turbines. J Eng Power 1982;104:44–50.

[60] Hall RJ, Smooke MD, Colket MB. Predictions of soot dynamics in opposed jet diffusion flames. Phys Chem Asp Combust A Tribut to Irvin Glas 1997;4:189–229.

[61] Raithby GD, Chui EH. A finite-volume method for predicting a radiant heat transfer in enclosures with participating media. J Heat Transfer 1990;112:415–23.

[62] Darbandi M, Abrar B. A compressible approach to solve combined natural convection-radiation heat transfer in participating media. Numer Heat Transf Part B Fundam

2014;66:446–69.

[63] Darbandi M, Abrar B. Thermal radiation transfer calculations in combustion fields using the SLW model coupled with a modified reference approach. J Quant Spectrosc Radiat Transf 2018;205:105–13.

[64] Wen Z, Yun S, Thomson MJ, Lightstone MF. Modeling soot formation in turbulent kerosene/air jet diffusion flames. Combust Flame 2003;135:323–40.

[65] Darbandi M, Schneider GE. Analogy-based method for solving compressible and incompressible flows. J Thermophys Heat Transf 1998;12:239–47.

[66] Darbandi M, Ghafourizadeh M. Extending a hybrid finite-volume-element method to solve laminar diffusive flame. Numer Heat Transf Part B Fundam 2014;66:181–210.

[67] Darbandi M, Ghafourizadeh M. Solving turbulent diffusion flame in cylindrical frame applying an improved advective kinetics scheme. Theor Comput Fluid Dyn 2015;29:413–31.

[68] Darbandi M, Ghafourizadeh M. A new bi-implicit finite volume element method for coupled systems of turbulent flow and aerosol-combustion dynamics. J Coupled Syst Multiscale Dyn 2016;4:43–59.

[69] Ebrahimi-Kebria H, Darbandi M, Hosseinizadeh SF. Numerical Simulation of Low-Mach-Number Laminar Mixing and Reacting Flows Using a Dual-Purpose Pressure-Based Algorithm. Numer Heat Transf Part B Fundam 2011;59:495–514.

[70] Darbandi M, Ghafourizadeh M. Extending a low-order upwind-biased scheme to solve turbulent flames using detailed chemistry model. Numer Heat Transf Part B Fundam 2018;73:343–62.

[71] Darbandi M, Abrar B. Advances in non-gray radiation calculation in combusting environments using a modified reference approach. Heat Mass Transf 2018;54:2705–13.

[72] Bordbar H, Hyppänen T. Line by line based band identification for non-gray gas modeling with a banded approach. Int J Heat Mass Transf 2018;127:870–84.

[73] Bordbar H, Maximov A, Hyppänen T. Improved banded method for spectral thermal radiation in participating media with spectrally dependent wall emittance. Appl Energy 2019;235:1090–105.

[74] Darbandi M, Abrar B, Barezban MB, Schneider GE, Shamsaei Y, Nematollahi M. On Radiative Heat Transfer Modeling in Numerical Simulation of a Heavy Duty Steam Generator. 54th AIAA Aerosp. Sci. Meet., 2016, p. 2151.

[75] Darbandi M, Ghafourizadeh M. Numerical study of inlet turbulators effect on the thermal characteristics of a jet propulsion-fueled combustor and its hazardous pollutants emission. J Heat Transfer 2017;139:61201.

[76] Darbandi M, Vakilipour S. Developing implicit pressure-weighted upwinding scheme to calculate steady and unsteady flows on unstructured grids. Int J Numer Methods Fluids 2008;56:115–41.

[77] Schneider GE, Raw MJ. Control volume finite-element method for heat transfer and fluid flow using colocated variables—1. Computational procedure. Numer Heat Transf Part A Appl 1987;11:363–90.

[78] Darbandi M, Schneider GE. Application of an all-speed flow algorithm to heat transfer problems. Numer Heat Transf Part A Appl 1999;35:695–715.

[79] Saario A, Rebola A, Coelho PJ, Costa M, Oksanen A. Heavy fuel oil combustion in a cylindrical laboratory furnace: measurements and modeling. Fuel 2005;84:359–69.